Appendix

Table of Content

Appendix Supplementary Methods

Molecular dynamics simulations

All molecular dynamics simulations were performed with the NAMD package (Phillips et al, 2005) with CHARMM force field (Best et al, 2012; Klauda et al, 2010): CHARMM36 for the lipid parameters, CHARMM27-cmap for the rest of the systems. Both equilibration and production runs were performed in the NPT ensemble (310 K, 1 bar, Nose-Hoover coupling scheme) with a time step of 2 fs. The particle mesh Ewald technique was used for the electrostatic calculations. The van der Waals and short-range electrostatic interactions were cut off at 12.0 Å with switch at 10.0 Å. CHARMM-GUI (Jo et al, 2008) was used to build the protein-membrane and protein-solvent systems. The lipid bilayer consist of the MOM characteristic phospholipids (Kuwana et al, 2002), including 46.5% L-α-phosphatidylcholine (PC), 28.4% L-α-phosphatidylethanolamine (PE), 8.9% L-α-phosphatidylinositol (PI), 8.9% L-α-phosphatidylserine (PS) and 7.3% cardiolipin. All systems were solvated with explicit water in TIP3P model in a periodic box. Counterions (Na^+ and Cl^-) were added to the systems. The system setups are listed in Appendix Table S1.

We have performed two equivalent metadynamics simulations (Iannuzzi et al, 2003; Laio & Parrinello, 2002), each in 30 ns, with NAMD package, for free energy change from the intersected to parallel α9 dimer, with the assumption that the transition between two conformations is reversible. The sampling bias was applied to two collective variables – the angles of rotation (α, β) around the principle axis of the monomeric helix. The results from the two replicates are consistent.

Appendix Tables

Table S1. Molecular dynamics simulation setups for α9 dimer and α2-α3-α4-α5 dimer.

Bax dimer	Box size ($Å^3$)	No. of atoms	No. of lipids in bilayer	No. of water molecules	Simulation length (ns)
Intersected α9 in membrane	77×77×69	37165	160	4711	175
Parallel α9 in membrane	77×77×69	37051	160	4673	175
Intersected to parallel α9 transition by metadynamics	77×77×69	37165	160	4711	30x2*
Intersected α9 in solvent	51×51×51	12264	0	3852	174
Parallel α9 in solvent	55×55×55	15504	0	4930	174
Intersected α9-G179I in membrane	77×77×69	37018	160	4654	70
Intersected α9-T182I in membrane	77×77×69	37046	160	4668	70
Parallel α9-G179I in membrane	77×77×69	37096	160	4680	70
Parallel α9-T182I in membrane	77×77×69	37088	160	4682	70
α2-α3-α4-α5 at membrane	73×73×97	47630	141	8557	135

* Two equivalent metadynamics simulations, each for 30 ns.

Appendix Figure Legends

Figure S1. Mitochondria-bound Bax proteins from the cytochrome c release assay.
Aliquots of the mitochondrial pellet fractions from the cytochrome c release assay were analyzed by reducing or non-reducing SDS-PAGE. The mitochondria-bound radioactive wild-type Bax protein or the indicated mutants that mediated the tBid-induced cytochrome c release shown in Figures EV1B-C, 9 and 10A were detected by phosphor-imaging, and indicated by circles on one side of the images. The protein standards are indicated on the other side with their M_r. The other minor radioactive protein bands are backgrounds produced by the TNT reactions. As expected, addition of tBid increased the binding of most of the Bax proteins to the mitochondria. The amount of Bax proteins bound to the mitochondria varied among the mutants; however, it was not correlated with the extent of cytochrome c release by the respective mutants in Figure EV1C and Figure 9 and 10A, suggesting that even the lower amounts of Bax were sufficient for the MOMP unless the protein was inactivated by mutations.

Figure S2. Reducing SDS-PAGE analysis of disulfide-crosslinked Bax proteins.
A-C. Aliquots of the crosslinked samples from Figure 1B-C, 3A-B, or 6B and 6D were analyzed by reducing SDS-PAGE and phosphor-imaging, and the results are shown in (A), (B), or (C), respectively.

Figure S3. Quantification of IASD labeling data, related to Figure 2.
A. The IASD labeling data from Bax L59C were shown to illustrate quantification procedures using the Multi Gauge program. To create a quantifying region, a rectangle was drawn to enclose a typical band, such as the rectangle c that encloses the IASD-labeled band in lane 3. Rectangles of the same size (a, b, d-j) were then used to enclose

the other nine bands (labeled and unlabeled) in lanes 1-5, and to enclose a region in which there is no band (rectangle-k), creating other quantifying regions. The amount of photo-stimulated luminescence (PSL) from each of the 11 quantifying regions was measured. The PSL value is in proportion to the amount of radiation emitted from the radioactive protein band and exposed to phosphor-imaging plate.

To correct for the uneven sample recovery and loading, the total PSL from the labeled and unlabeled bands in each lane was divided by the total PSL from the labeled and unlabeled bands in lane 1 to obtain the normalization factor for each sample. The PSL from each of the 10 labeled and unlabeled bands was normalized by the corresponding normalization factor. Using the IASD-labeling sample in lane 2 as an example,

Normalization factor = [PSL(b) + PSL(g)] / [PSL(a) + PSL(f)]

Normalized PSL(b) = PSL(b) / Normalization factor

Normalized PSL(g) = PSL(g) / Normalization factor

To calculate the net PSL of each of the IASD-labeled bands, subtract the normalized PSL of the labeled band in lane 1 from the normalized PSL of the corresponding labeled band. This is based on an assumption that the IASD labeling should not occur in the sample in lane 1, as IASD should be quenched by β-mecaptoethanol that was already present in the sample before the addition of IASD. Any PSL from rectangle-a would result from an IASD-independent modification of the Bax protein that would also occur in the other samples, and hence, must be subtracted.

To calculate the net PSL of each of the unlabeled bands, subtract the PSL of rectangle-k from the normalized PSL of the corresponding unlabeled band. This is because there is no band in rectangle-k; any PSL from there must be from the background that would also be present in other rectangles enclosing the unlabeled bands, and hence, must be deducted. Using the IASD-labeling sample in lane 2 as an example,

Net PSL (b) = Normalized PSL (b) – Normalized PSL (a)

Net PSL (g) = Normalized PSL (g) – PSL (k)

To calculate the fraction of IASD-labeling, divide the net PSL of a labeled band by the sum of the net PSL's of the labeled band and the corresponding unlabeled band. Using the IASD-labeling sample in lane 2 as an example,

Fraction of IASD-labeling (2) = Net PSL (b) / [Net PSL (b) + Net PSL (g)]

To calculate the membrane burial index, subtract the fraction of IASD-labeling from the reaction performed in the presence of urea (lane 4) from the fraction of IASD-labeling from the reaction performed in the presence of both urea and CHAPS (lane 5). This is because the urea in both samples should denature the protein or the protein complex, exposing the protein-buried cysteine to IASD. The difference between the fractions of IASD-labeling from the two reactions must be due to the CHAPS in the second reaction that solubilizes the MOM, exposing the MOM-buried cysteine to IASD. Thus,

membrane burial index (Bax L59C) = Fraction of IASD-labeling (5) – Fraction of IASD-labeling (4)

To calculate the protein burial index, subtract the fraction of IASD-labeling from the reaction performed in the presence of CHAPS (lane 3) from the fraction of IASD-labeling from the reaction performed in the presence of both urea and CHAPS (lane 5). This is because CHAPS in both samples should solubilize the MOM, exposing the MOM-buried cysteine to IASD. The difference between the fractions of IASD labeling from the two reactions must be due to the urea in the second reaction that denatures the protein or the protein complex, exposing the protein-buried cysteine to IASD. Thus,

Protein burial index (Bax L59C) = Fraction of IASD-labeling (5) – Fraction of IASD-labeling (3)

B-C. The phosphor-imaging data for IASD labeling of Bax mutants in Figure 2B and the similar data from the independent replicates were quantified as described in (A). The

membrane (B) or protein (C) burial indices were derived and shown as the dots with the lines for the means.

Figure S4. Molecular dynamics simulation of the BH3-in-groove dimer on the membrane after helix α5 inserts into the membrane.

A. The initial structure in tube representation was generated from the BH3-in-groove dimer structure (PDB entry 4BDU) with the α2-α3-α4 part remained on the membrane surface and the α5 part released into the lipid bilayer. The final structure at t = 135 ns is shown in cartoon representation. One monomer is shown with α2 in green, α3 in magenta, α4 in blue, and α5 in red, while the other monomer is colored in gray, consistent with the color codes assigned in Figure 1A. The lipids in the membrane and the surrounding waters are presented as lines and van der Waals' beads, respectively.

B. Time evolutions of the β carbon distances between the indicated residue pairs in the BH3-in-groove dimer during the molecular dynamics simulation described in (A). Within 135 ns the β carbon distance between L76 in one monomer and L59' in the other monomer reached below 6 Å constantly, whereas the distance between E69 and E69' or between S55 and R94' reached below 6 Å occasionally. However, the distance between S62 and S72' remained above 10 Å.

Figure S5. Quantification of IASD labeling data from Bax mutants with single cysteine in helix α9, related to Figure 5.

A-B. The phosphor-imaging data for IASD labeling of Bax mutants in Figure 5A and the similar data the independent replicates were quantified as described in Appendix Figure S3A. The membrane (A) or protein (B) burial indices were derived and shown as the dots with the lines for the means.

Figure S6. Molecular dynamics simulations of helix α9 dimers without or with G179I or T182I mutation.

A. Comparison of initial and final conformations of two α9 dimers simulated in the membrane and solution. Initial conformations at *t* = 0 ns are shown in tube representation, to which the final conformations at *t* = 175 ns in cartoon representation are superimposed. As indicated by the backbone RMSD between the initial and final conformations, both intersected and parallel α9 dimers display relatively high stability in the membrane, but they are unstable in the solution and lose helicity from both termini.

B. Metadynamics simulation of free-energy of α9 dimer transition between parallel (I) and intersected (IV) conformational states. II and III are intermediate states. The intersected state has the lowest relative free-energy, which is set to be zero. The relative free-energy (kcal/mol) of the other states are indicated under the structures. The contact residues in the intersected dimer observed in the crosslinking experiments are shown as red sticks, while those in the parallel dimer are depicted as green sticks. The backbone RMSD of conformations I, II, III, and IV, if comparing with I, are 0, 2.8, 3.3, and 5.2 Å; and if comparing with IV, are 5.2, 3.2, 3.3 and 0 Å, respectively.

C. The initial intersected and parallel α9 dimer structures at t = 0 ns are shown on the left side of each panel as light orange cartoons with the mutated residues G179I and T182I highlighted as spheres. The final structures at t = 45 ns are shown on the right side as pink and blue cartoons. Within the simulation time, the G179I mutation disrupts both intersected and parallel dimer conformations, while T182I mutation only disrupts the parallel dimer conformation, as indicated by the > 2-fold increase of β carbon distance (Å) between A183 and A183' (linked by a red dashed line with the distance value) or

between A178 and A178' (linked by a blue dashed line with the distance value) from the initial to the final structure.

Figure S7. G179I mutation enhances membrane insertion of α9, related to Figure 10.

A-B. The phosphor-imaging data for IASD labeling of Bax mutants in Figure 10D and the similar data from the independent replicates were quantified as described in Appendix Figure S3A. The membrane or protein burial indices were derived and shown in (A) as the dots with the lines for the means. The relative protein burial indices were then obtained as described in Figure 2D and shown in (B).

Appendix References

Best RB, Zhu X, Shim J, Lopes PE, Mittal J, Feig M, Mackerell AD, Jr. (2012) Optimization of the additive CHARMM all-atom protein force field targeting improved sampling of the backbone phi, psi and side-chain chi(1) and chi(2) dihedral angles. *Journal of chemical theory and computation* **8:** 3257-3273

Iannuzzi M, Laio A, Parrinello M (2003) Efficient exploration of reactive potential energy surfaces using Car-Parrinello molecular dynamics. *Phys Rev Lett* **90:** 238302

Jo S, Kim T, Iyer VG, Im W (2008) CHARMM-GUI: a web-based graphical user interface for CHARMM. *Journal of computational chemistry* **29:** 1859-1865

Klauda JB, Venable RM, Freites JA, O'Connor JW, Tobias DJ, Mondragon-Ramirez C, Vorobyov I, MacKerell AD, Jr., Pastor RW (2010) Update of the CHARMM all-atom additive force field for lipids: validation on six lipid types. *J Phys Chem B* **114:** 7830-7843

Kuwana T, Mackey MR, Perkins G, Ellisman MH, Latterich M, Schneiter R, Green DR, Newmeyer DD (2002) Bid, Bax, and lipids cooperate to form supramolecular openings in the outer mitochondrial membrane. *Cell* **111:** 331-342

Laio A, Parrinello M (2002) Escaping free-energy minima. *Proc Natl Acad Sci U S A* **99:** 12562-12566

Phillips JC, Braun R, Wang W, Gumbart J, Tajkhorshid E, Villa E, Chipot C, Skeel RD, Kale L, Schulten K (2005) Scalable molecular dynamics with NAMD. *Journal of computational chemistry* **26:** 1781-1802

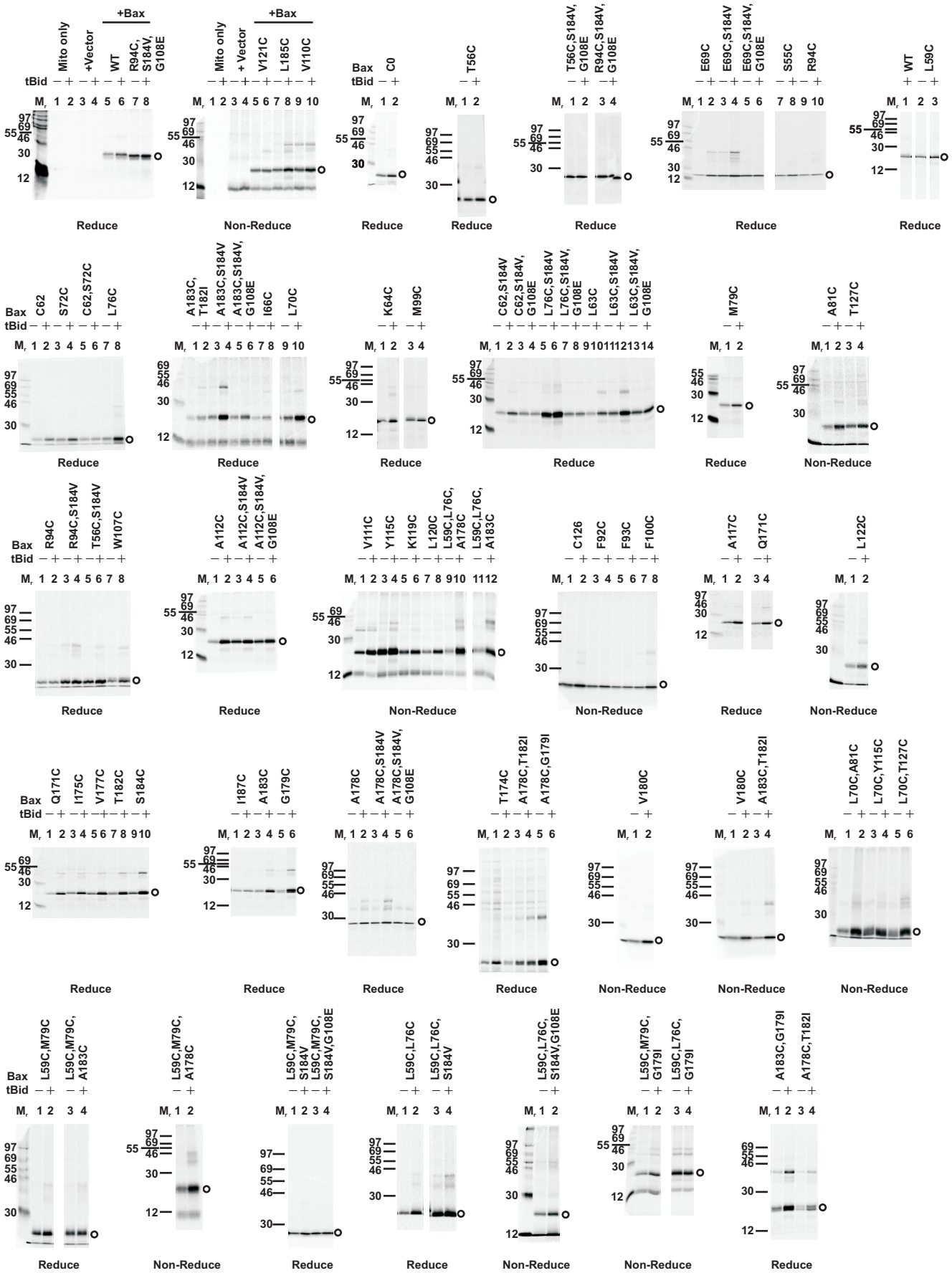

Appendix Figure S1

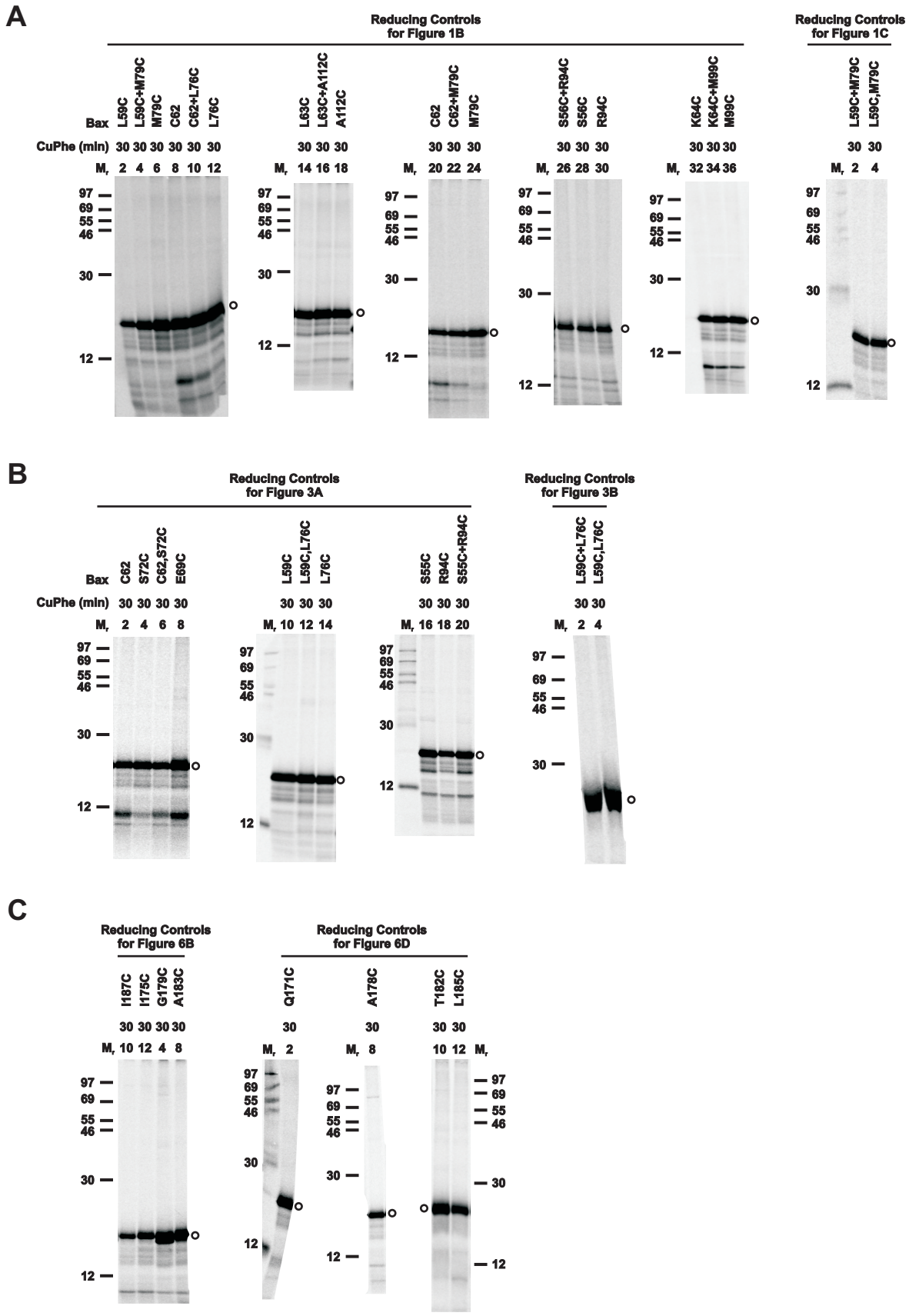

Appendix Figure S2

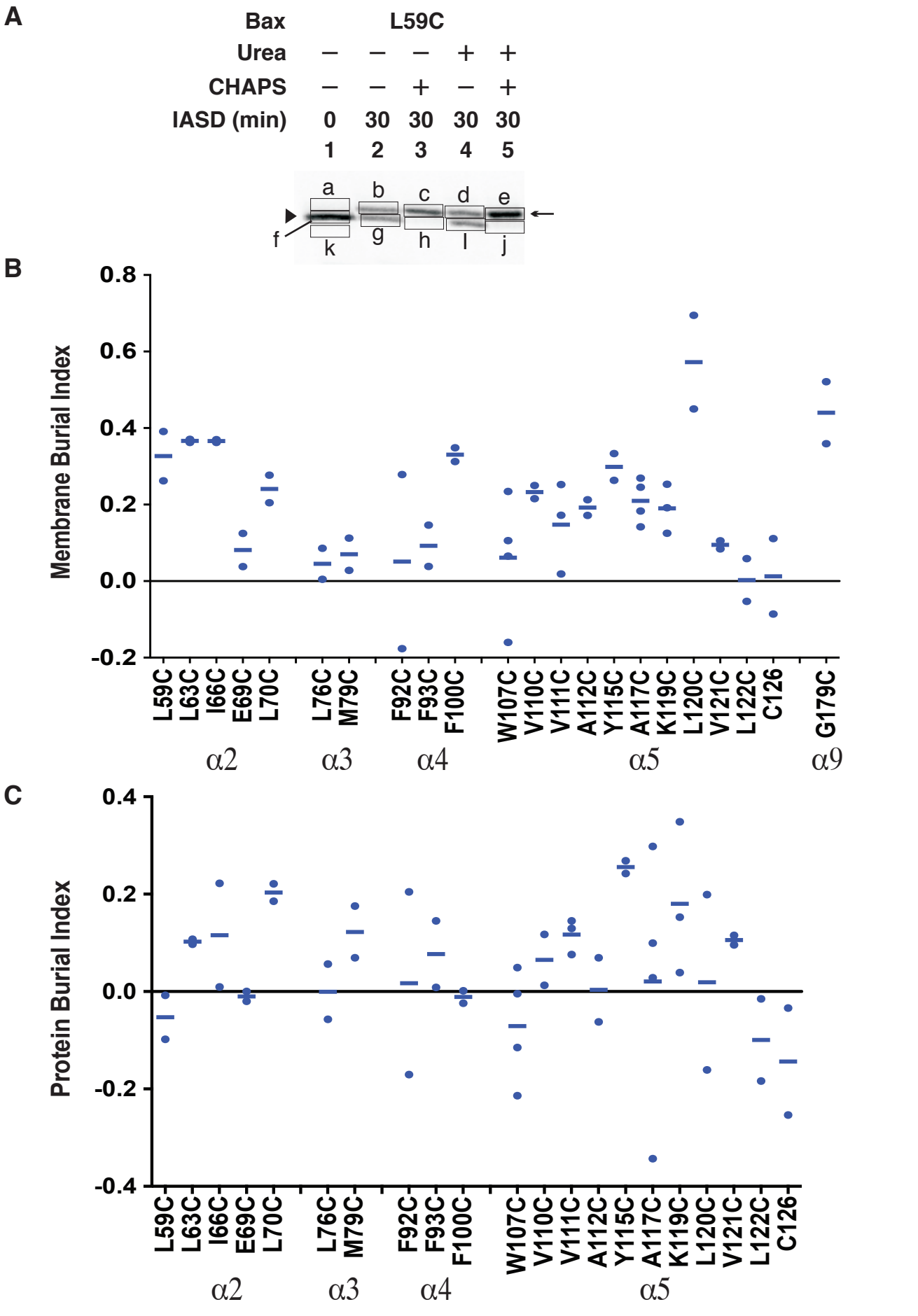

Appendix Figure S3

A

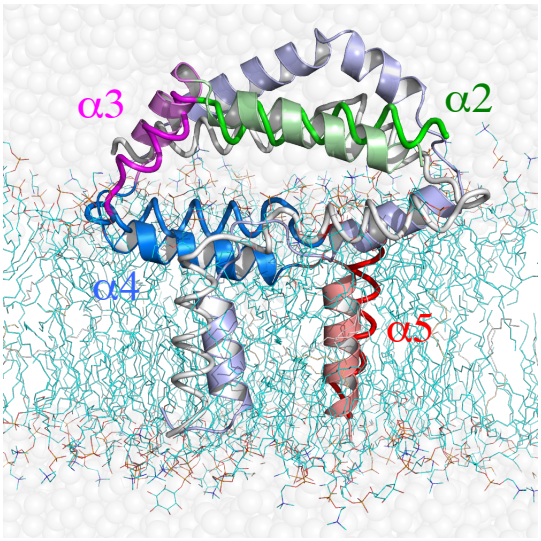

B

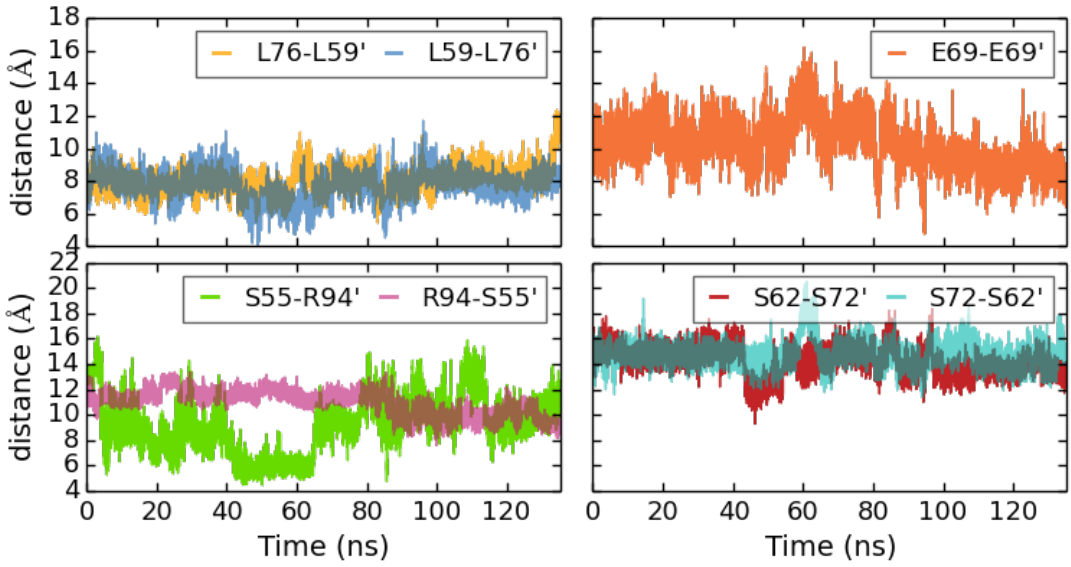

Appendix Figure S4

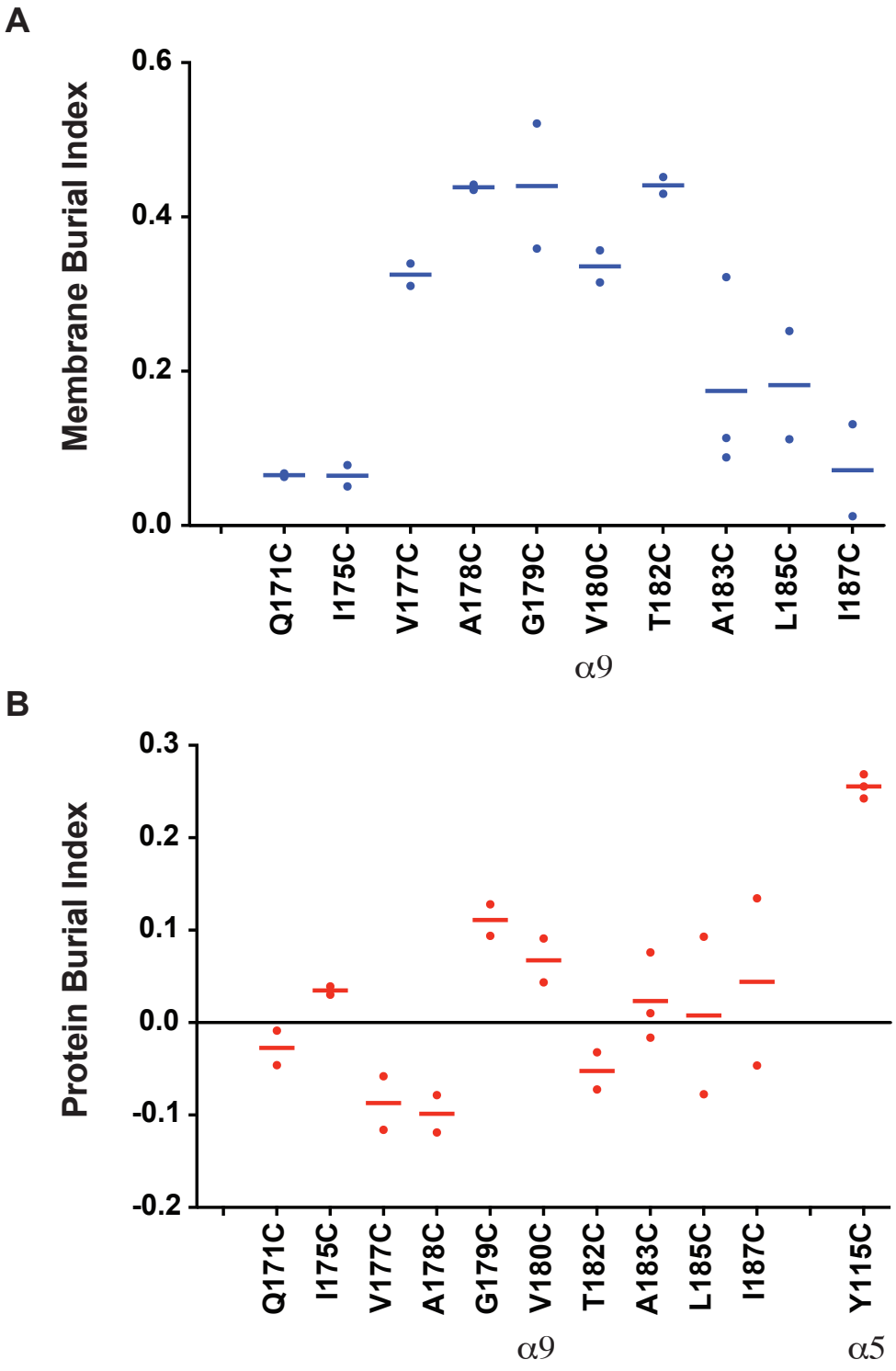

Appendix Figure S5

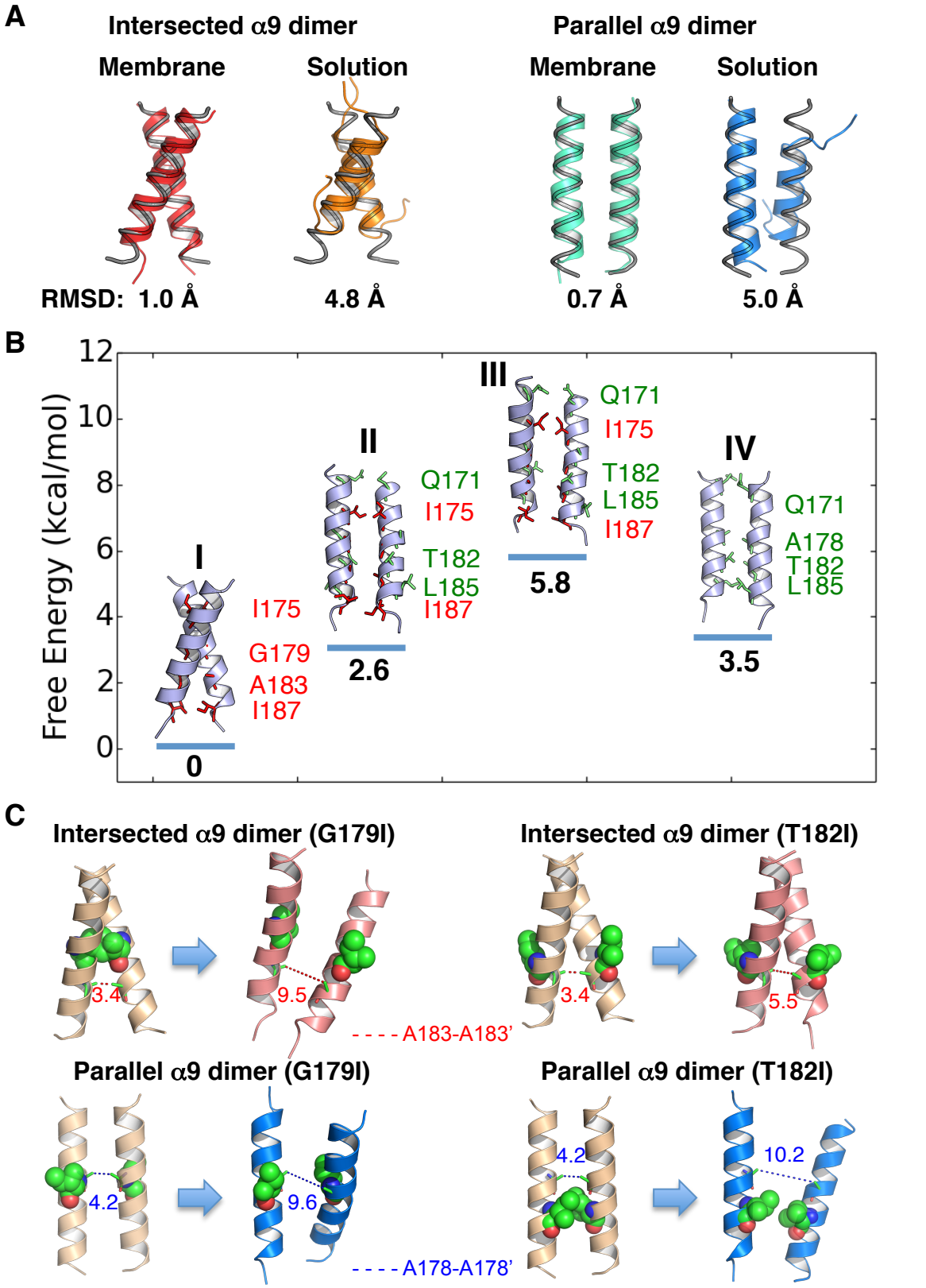

Appendix Figure S6

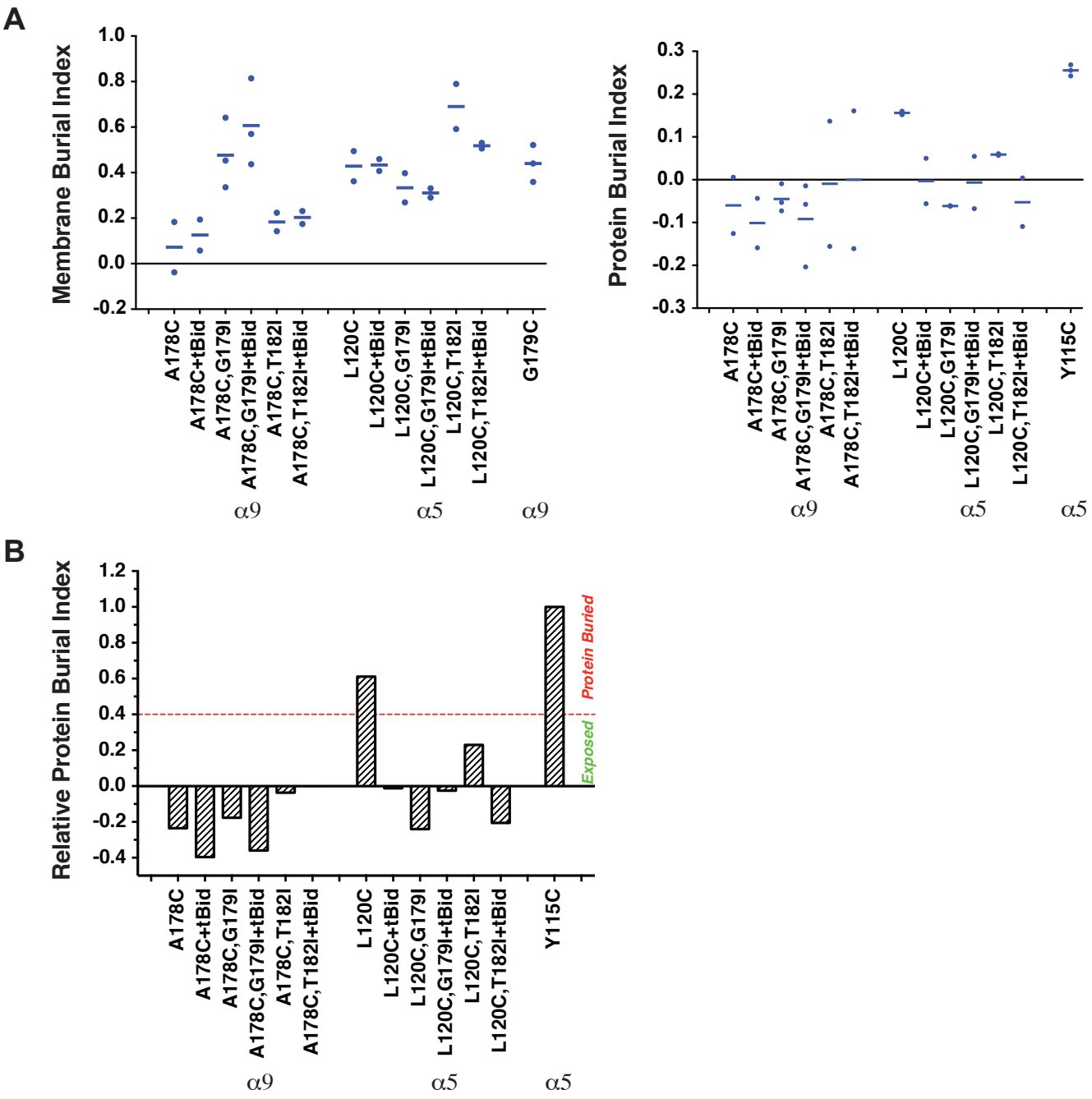

Appendix Figure S7